An Interior Point Iterative Maximum-Likelihood Reconstruction Algorithm Incorporating Upper and Lower Bounds with Application to SPECT Transmission Imaging

Manoj V. Narayanan*, *Associate Member, IEEE*, Charles L. Byrne, *Member, IEEE*, and Michael A. King, *Senior Member, IEEE*

Abstract—**The algorithm we consider here is a *block-iterative* (or *ordered subset*) version of the *interior point algorithm* for transmission reconstruction. Our algorithm is an *interior point* method because each vector of the iterative sequence $\{x^k\}, k = 0, 1, 2, \ldots$ satisfies the constraints $a_j < x_j^k < b_j, j = 1, \ldots, J$. Because it is a block-iterative algorithm that reconstructs the transmission attenuation map and places constraints above and below the pixel values of the reconstructed image, we call it the BITAB method. Computer simulations using the three-dimensional mathematical cardiac and torso phantom, reveal that the BITAB algorithm in conjunction with reasonably selected prior upper and lower bounds has the potential to improve the accuracy of the reconstructed attenuation coefficients from truncated fan beam transmission projections. By suitably selecting the bounds, it is possible to restrict the over estimation of coefficients outside the fully sampled region, that results from reconstructing truncated fan beam projections with iterative transmission algorithms such as the maximum-likelihood gradient type algorithm.**

Index Terms—**Attenuation, iterative methods, single photon emission computed tomography.**

I. Introduction

PATIENT-SPECIFIC single photon emission computed tomography (SPECT) attenuation maps have been reconstructed using fan beam transmission tomography to correct for nonuniform attenuation in cardiac perfusion imaging [1]–[8]. One such SPECT system consists of three camera heads with a fan beam collimator opposed to a line source acquiring transmission images, while two parallel beam collimators on the other two heads acquire emission images simultaneously [1], [3], [7]. However, transmission imaging with a symmetric fan beam collimator on a standard gamma camera with a useful field of view (FOV) of 40 cm, generally results in projection data that are truncated in many views [8]. This leads to incomplete sampling of regions of what would have been the FOV had a parallel hole collimator been employed.

To improve the accuracy of the reconstructed transmission maps in the presence of truncation, investigators have proposed maximum *a posteriori* (MAP) algorithms [4] that provide some form of regularization using suitably chosen priors. Extrapolating the truncated projections using body outlines has also been proposed to reduce truncation artifacts [9]–[12]. Other efforts on three-headed SPECT systems include, enlarging the fully sampled region (FSR) through longer focal-length symmetric fan-beam collimators [5] or asymmetric fan-beam collimators [13]–[15]. Additionally, slant hole collimators have also been proposed [16] as a way to obtain truncation-free attenuation maps of large patients on a three headed SPECT system.

In this paper, we develop an accelerated block-iterative version of a new iterative interior point optimization algorithm (IPA) developed by Byrne [17]. We then apply this block-iterative algorithm to SPECT transmission imaging. The resulting algorithm is related to the rescaled block-iterative version of the expectation-maximization maximum-likelihood method (RBI-EM) [18], [19] and is similar to the algorithms presented in [20] in that it includes prior upper and lower bound information. Because it is a block-iterative algorithm that reconstructs the transmission attenuation map and places constraints above and below the pixel values of the reconstructed image, we call it the BITAB method. We shall show through computer simulations, phantom and clinical patient studies that the BITAB algorithm, in conjunction with reasonably selected prior upper and lower bounds, has the potential to improve the accuracy of the reconstructed attenuation coefficients from truncated fan beam transmission projections. In addition, due to its block-iterative formulation, the BITAB algorithm also reduces reconstruction times considerably. The BITAB algorithm is presented in Section II, while Section III discusses computer simulation experiments along with phantom and patient studies. A discussion of the results along with conclusions are presented in Sections IV and V.

Manuscript received October 9, 1998; revised February 7, 2001. The Associate Editor responsible for coordinating the review of this paper and recommending its publication was J. A. Fessler. *Asterisk indicates corresponding author.*

*M. V. Narayanan is with the Division of Nuclear Medicine, Department of Radiology, University of Massachusetts Medical School, 55 Lake Avenue N., Worcester MA 01655 USA (e-mail: Manoj.Narayana@umassmed.edu).

C. L. Byrne is with the the Department of Mathematical Sciences, University of Massachusetts at Lowell, Lowell, MA 01854 USA.

M. A. King is with the Division of Nuclear Medicine, Department of Radiology, University of Massachusetts Medical School, Worcester MA 01655 USA (e-mail: Manoj.Narayana@umassmed.edu).

Publisher Item Identifier S 0278-0062(01)03551-0.

II. The BITAB Algorithm for SPECT Transmission Image Reconstruction

In this section, we discuss briefly the interior point algorithm (IPA) and then consider the BITAB algorithm, which is a special case of the IPA, used to maximize the likelihood function associated with transmission tomography data, subject to upper and lower constraints on the pixels.

A. The Interior Point Algorithm (IPA)

The interior point algorithm (IPA) given in [17] is an iterative procedure for minimizing a convex function $h(x)$ over variables x constrained to lie within the domain of definition, C, of a second (Bregman) function $f(x)$ (see the Appendix for a discussion of Bregman functions). With the selection of the function $f(x)$ we impose desired constraints on the reconstructed image. In general, let f be a Bregman function. Let $h(x)$ be a differentiable convex function on R^J. The IPA is now the following:

Algorithm II.1: Let $r > 0$ be arbitrary. Having calculated x^k we solve

$$\nabla f(x^{k+1}) + r\nabla h(x^{k+1}) = \nabla f(x^k) \tag{2.1}$$

for x^{k+1}.

We have the following result (see [17]).

Theorem II.1: Assume that the minimum of h on C is attained, where C is the domain of f. If we can solve (2.1) for x^{k+1}, for each $k = 0, 1, \ldots$, then the sequence $\{h(x^k)\}$ is decreasing and the sequence $\{x^k\}$ converges to a minimizer of h over the set C.

One drawback to using the IPA is the difficulty in solving the gradient (2.1). We can rewrite the IPA iterative step in (2.1) in a way that leads to a more computationally tractable iterative step. Instead of (2.1) we write

$$\nabla F(x^{k+1}) = \nabla F(x^k) - r\nabla h(x^k) \tag{2.2}$$

using $F(x) = f(x) + rh(x)$. Note that this is the same iterative step; we are not using a 'one-step-late' approximation, but only introducing new notation. Suppose that we then select $F(x)$ *a priori* to permit easy inversion. If we choose $r > 0$ so that the function $f(x) = F(x) - rh(x)$ is a Bregman function, the iteration in (2.2) converges. As before, the sequence $\{h(x^k)\}$ is decreasing; the iteration is a true descent method, even though the constant r is not updated at each step.

For example, let $F(x) = (1/2)\|x\|^2$, half the Euclidean norm squared. Then (2.2) becomes

$$x^{k+1} = x^k - r\nabla h(x^k). \tag{2.3}$$

The behavior of this algorithm is considered in more detail in [17].

In order to obtain reconstructed images $x = (x_1, \ldots, x_J)^T$ with $a_j \le x_j \le b_j$, for $j = 1, \ldots, J$, we shall use the Bregman function $F(x) = F_{ab}(x)$ given by

$$F_{ab}(x) = \sum_{j=1}^{J} (x_j - a_j)\log(x_j - a_j) + (b_j - x_j)\log(b_j - x_j). \tag{2.4}$$

To accelerate production of a useful reconstructed image, we incorporate the rescaled block-iterative technique, as well. We partition the index set $\{i = 1, \ldots, I\}$ into N disjoint blocks, $B_n, n = 1, \ldots, N$. Then, at the k-th step and with $n = k(\mathrm{mod}\, N) + 1$, we solve

$$\nabla F_{ab}(x^{k+1}) = \nabla F_{ab}(x^k) - r\nabla h_n(x^k) \tag{2.5}$$

where $h_n(x)$ is related to $h(x)$, but depends only on the data values y_i for i in B_n, the nth block. The algorithm we obtain is the following: having calculated x^k, let x^{k+1} be determined by (2.5). Then we have

$$x_j^{k+1} = \left[A_j^k a_j + B_j^k b_j\right] / \left[A_j^k + B_j^k\right] \tag{2.6}$$

where

$$A_j^k = b_j - x_j^k \tag{2.7}$$

and

$$B_j^k = \left(x_j^k - a_j\right)\exp\left(-r\frac{\partial h_n}{\partial x_j}(x^k)\right). \tag{2.8}$$

Now we consider a special case of the IPA obtained by selecting particular functions F and h.

B. The BITAB Algorithm for Transmission Image Reconstruction

For the case of transmission image reconstruction we can write the regularized log-likelihood function as

$$\mathrm{RLL}(x) = \sum_i y_i \ln[c_i \exp(-(Lx)_i) + s_i] - c_i \exp(-(Lx)_i) + \beta U(x) + \text{constants}$$

where

y_i	count at detector i;
L_{ij} of matrix L	length of the intersection of the ith line segment with the jth pixel;
$(Lx)_i$	$= \sum_j L_{ij}x_j$;
constant $c_i > 0$	input intensity along the ith segment;
s_i	estimate of the scatter component in the data y_i;
$U(x)$	penalty function used for regularization;
β	regularization parameter.

Alternatively, we can rewrite $\mathrm{RLL}(x)$ in terms of a function $h(x)$ given by

$$h(x) = \sum_i KL(y_i, c_i \exp(-(Lx)_i) + s_i) + \beta U(x)$$

where for nonnegative scalars u and v, we denote $KL(u, v) = u\log(u/v) + v - u$. Since $h(x)$ is equivalent to the regularized negative log-likelihood function with some additional constants, our objective would be to minimize $h(x)$. The algorithm we consider here is a block-iterative (or ordered subset) version of the IPA. Our algorithm is an interior point method because each vector of the iterative sequence $\{x^k\}, k = 0, 1, 2, \ldots$ satisfies the constraints $a_j < x_j^k < b_j, j = 1, \ldots, J$.

For the block-iterative version we let $h_n(x)$ be

$$h_n(x) = \sum^n KL(y_i, c_i \exp(-(Lx)_i) + s_i) + \hat{\beta}U(x), \tag{2.9}$$

where $\sum^n$ denotes the sum over indices i in B_n. Note that as suggested by [25], for the ordered subset case, the regularization parameter $\hat{\beta} = \beta/N$ where N is the total number of disjoint subsets. Then we get the BITAB algorithm where x_j^{k+1} and A_j^k are defined in (2.6) and (2.7), respectively, with (2.10), shown at the bottom of the page, for suitable $r > 0$.

We do not expect block-iterative methods to converge to a single image, in the presence of noisy data. Instead, we usually obtain subsequence convergence to a limit cycle, consisting of as many separate images as there are blocks of data. How distinct these images are will depend on the signal-to-noise level in the data. For the simultaneous algorithm, in which we put all the data into a single block, the theory of the IPA tells us that, provided we choose r so that the function $F(x) - rh(x)$ is a Bregman function, the sequence $\{h(x^k)\}$ is decreasing and the sequence $\{x^k\}$ converges to a constrained minimizer of the function $h(x)$. The most important property to be checked is that this function be convex. We shall obtain an upper limit on the acceptable values of r by considering the Hessian matrix of this function. For this purpose we shall ignore the regularization term $\beta U(x)$ in $h(x)$.

With $F(x) = F_{ab}(x)$ and $h(x) = \sum_i KL(y_i, c_i \exp(-(Lx)_i))$ the Hessian matrix of $F_{ab}(x)$ is

$$\nabla^2 F_{ab}(x) = \text{diag}\{(x_j - a_j)^{-1} + (b_j - x_j)^{-1}\}. \quad (2.11)$$

The Hessian matrix of $h(x)$ is

$$\nabla^2 h(x) = L^T W L \quad (2.12)$$

where $W = \text{diag}\{c_i \exp(-(Lx)_i)\}$. The smallest eigenvalue of $\nabla^2 F_{ab}(x)$ is the minimum, over all j, of $(x_j - a_j)^{-1} + (b_j - x_j)^{-1}$. Since

$$(x_j - a_j)^{-1} + (b_j - x_j)^{-1} \geq \frac{4}{b_j - a_j} \quad (2.13)$$

we know that the smallest eigenvalue of $\nabla^2 F_{ab}(x)$ is not smaller than the minimum, over all j, of $4/(b_j - a_j)$.

The trace of the matrix $\nabla^2 h(x)$, which is the sum of its eigenvalues, is

$$\text{trace}\nabla^2 h(x) = \sum_i \left(\sum_j L_{ij}^2 \right) c_i \exp(-(Lx)_i). \quad (2.14)$$

Hence, for vectors x with $a_j \leq x_j \leq b_j, j = 1, \ldots, J$, we have

$$\text{trace}\nabla^2 h(x) \leq \sum_i \left(\sum_j L_{ij}^2 \right) c_i \exp(-(La)_i). \quad (2.15)$$

Therefore, the Hessian of $F_{ab}(x) - rh(x)$ will be positive-definite if the constant $r > 0$ satisfies the inequality

$$r \leq 4 \min_j \left\{ \frac{1}{b_j - a_j} \right\} \Big/ \sum_i \left(\sum_j L_{ij}^2 \right) c_i \exp(-(La)_i) \quad (2.16)$$

where $a = (a_1, \ldots, a_J)^T$. Note however, that the value of r as specified by (2.16) often is quite conservative. Equation (2.16) serves as a reasonable starting-point for choosing r. Indeed, our simulation and clinical results indicate that choosing r in the range of 5 to 15 provides good results for transmission reconstructions.

In the simultaneous case, with only a single block, if $F(x) - rH(x)$ is a Bregman function, we have that the sequence $\{h(x^k)\}$ is decreasing and that the sequence $\{x^k\}$ converges to a minimizer of the function $h(x)$, subject to the constraints $a_j \leq x_j \leq b_j$. In the case of more than one block, we do not expect $\{h(x^k)\}$ to be decreasing, nor will the sequence $\{x^k\}$ converge to a single vector. Instead, we expect but have not proven that, for each $t = 0, 1, \ldots, N-1$ the subsequence $\{x^{mN+t}, m = 0, 1, \ldots\}$ will converge to a vector $x^{\infty,t}$. Based on empirical observations, the vectors $\{x^{\infty,t}, t = 0, 1, \ldots, N-1\}$ appear to form a *limit cycle*. The final reconstruction could be some sort of average (arithmetic or geometric) of the images constituting the limit cycle.

The convergence proof for the simultaneous case is based on the assumption that the objective function being minimized is convex. When crosstalk is included, the algorithm performs better, but the objective function is now convex on a portion of its domain only. So, for this reason also, the algorithm appears somewhat *ad hoc*. We take the view that, since a theorem asserting cyclic convergence of the block-iterative algorithm in the inconsistent case is (probably) beyond our reach, with or without the assumption of convexity, the theory acts more as a guide than as a foundation. We choose to prove what we can, under a reasonable set of assumptions, even though slight violations of those assumptions will be tolerated in the algorithm as implemented.

C. An Example of BITAB Using a Gamma Prior Distribution

We present now a special case of the BITAB algorithm, in which we use as our penalty function $U(x) = KL(p, x)$ where p is a prior estimate of the desired solution. This is equivalent to modifying the likelihood function to include a gamma distributed prior [21]. Again, with x_j^{k+1} and A_j^k defined in (2.6) and (2.7), respectively, the resulting algorithm is complete with (2.17), shown at the bottom of the next page, for suitable $r > 0$. This is the version of the BITAB that we investigate in this paper.

$$B_j^k = (x_j^k - a_j) \exp\left(-r \sum^n \left\{ L_{ij} \left[\frac{y_i \times c_i \exp(-(Lx^k)_i)}{c_i \exp(-(Lx^k)_i) + s_i} - c_i \exp(-(Lx^k)_i) \right] \right\} - r\hat{\beta} \frac{\partial U}{\partial x_j}(x^k) \right) \quad (2.10)$$

III. ML-G Algorithm

The maximum-likelihood gradient type (ML-G) algorithm is an efficient transmission algorithm proposed by Lange *et al.*, [22] and has the following form

$$x_j^{k+1} = x_j^k \frac{\sum_i L_{ij} c_i \exp(-(Lx^k)_i)}{\sum_i L_{ij} y_i}. \tag{3.18}$$

The algorithm in (3.18) cannot guarantee the increase of the likelihood function as the iteration proceeds: however, this is remedied by taking a fractional step in the direction of the increment $d^{k+1} = x^{k+1} - x^k$. Instead of using (3.18) to define the next vector in the iterative sequence, we use

$$x^{k+1} = x^k + \alpha d^{k+1} \tag{3.19}$$

where α is a relaxation parameter. ML-G reconstructions for both simulations and clinical studies used $\alpha = 0.4$ [2] as the relaxation parameter. The ML-G algorithm can be regularized by including Bayesian gamma priors [22]. Case *et al.*, [4] have shown that the modified ML-G algorithm of Lange *et al.*, [22] can be simplified to

$$\begin{aligned} x_j^{k+1} &= (1 - w_j) \\ &\quad \times \left(x_j^k + \alpha \left\{ x_j^k \frac{\sum_i L_{ij} c_i \exp(-(Lx^k)_i)}{\sum_i L_{ij} y_i} - x_j^k \right\} \right) \\ &\quad + w_j p_j \end{aligned} \tag{3.20}$$

where p_j is a prior estimate such as a segmented attenuation map, while w_j represents the pixel-by-pixel weighting given to the prior p_j. In this application, the prior estimate p is obtained by first computing the patient body-outline and then assigning soft-tissue attenuation coefficients to all pixels enclosed within the body-outline. For the fan-beam geometry under consideration, we assume that the ML-G reconstructions accurately represent the attenuation within the FSR; hence, very little weight is given to the prior p_j. Outside the FSR, where truncation artifacts dominate, more weight is given to the prior estimate. By spatially varying the weight w_j on a pixel-by-pixel basis it has been shown previously [4] that some of the distortions introduced by truncation could be reduced.

IV. Convex Algorithm

The Convex algorithm is another iterative transmission algorithm put forth by Lange *et al.* [23]. The objective here is to minimize the function $\sum_{i=1}^{I} KL(y_i, c_i \exp(-Lx_i))$. The convex algorithm uses the idea of substitute functions suggested by DePierro for emission tomography [24].

For each $k = 0, 1, \ldots$, we minimize

$$G_k(x) = \sum_{j=1}^{J} \sum_{i=1}^{I} \frac{L_{ij} x_j^k}{Lx_i^k} KL\left(y_i, c_i \exp\left(-x_j Lx_i^k / x_j^k\right)\right). \tag{4.21}$$

Setting the gradient to zero gives

$$0 = \sum_{i=1}^{I} L_{ij} \left(y_i - c_i \exp\left(-x_j Lx_i^k / x_j^k\right)\right). \tag{4.22}$$

One step of the Newton–Raphson method gives the convex algorithm

$$\begin{aligned} x_j^{k+1} &= x_j^k - x_j^k \frac{\sum_i L_{ij} \left(y_i - c_i \exp\left(-Lx_i^k\right)\right)}{\sum_i L_{ij} Lx_i^k c_i \exp\left(-Lx_i^k\right)} \\ &= x_j^k \frac{\sum_i L_{ij} \left(c_i \exp\left(-Lx_i^k\right)\left[1 + Lx_i^k\right] - y_i\right)}{\sum_i L_{ij} Lx_i^k c_i \exp\left(-Lx_i^k\right)}. \end{aligned} \tag{4.23}$$

Now we consider a gamma-prior variant of this method. The objective now is to minimize the function $\sum_{i=1}^{I} KL(y_i, c_i \exp(-Lx_i)) - S(x)$, where $S(x) = \sum_{j=1}^{J} [(\alpha_j - 1) \ln x_j - \alpha_j x_j / \beta_j]$ is the log gamma prior, β_j is the mean of the gamma distribution, and α_j is related to the variance. Since the penalty function $S(x)$ is already separable, we do not use DePierro's trick on that part.

For each $k = 0, 1, 2, \ldots$, we minimize the function $H_k(x) = G_k(x) - S(x)$, or

$$\begin{aligned} H_k(x) &= \sum_{j=1}^{J} \sum_{i=1}^{I} \frac{L_{ij} x_j^k}{Lx_i^k} KL\left(y_i, c_i \exp\left(-x_j Lx_i^k / x_j^k\right)\right) \\ &\quad - \sum_{j=1}^{J} [(\alpha_j - 1) \ln x_j - \alpha_j x_j / \beta_j]. \end{aligned} \tag{4.24}$$

Setting the gradient to zero gives

$$\begin{aligned} \nabla H_f(x)_j = 0 &= \sum_{i=1}^{I} L_{ij} \left(y_i - c_i \exp\left(-x_j Lx_i^k / x_j^k\right)\right) \\ &\quad + \alpha_j / \beta_j - (\alpha_j - 1) / x_j. \end{aligned} \tag{4.25}$$

One step of the Newton-Raphson method gives the desired algorithm is shown in (4.26) at the bottom of the page. Since the prior estimate p_j can be expressed in terms of the two parameters of the gamma distribution as $p_j = \beta_j(\alpha_j - 1)/\alpha_j$ [4], [22],

$$B_j^k = \left(x_j^k - a_j\right) \exp\left(-r \sum^{n} \left\{ L_{ij} \left[\frac{y_i \times c_i \exp(-(Lx^k)_i)}{c_i \exp(-(Lx^k)_i) + s_i} - c_i \exp(-(Lx^k)_i) \right] \right\} - r\hat{\beta} \frac{x_j^k - p_j}{x_j^k} \right) \tag{2.17}$$

$$x_j^{k+1} = x_j^k - x_j^k \frac{\left[\sum_i L_{ij} x_j^k \left(y_i - c_i \exp\left(-Lx_i^k\right)\right)\right] + \alpha_j x_j^k / \beta_j - (\alpha_j - 1)}{\left[\sum_i L_{ij} x_j^k Lx_i^k c_i \exp\left(-Lx_i^k\right)\right] + \alpha_j - 1} \tag{4.26}$$

see (4.27) at the bottom of the page. Note that for large values of α_j/β_j the next iterate x_j^{k+1} does not equal p_j. If instead of performing one Newton-Raphson step for $\nabla H_f(x)_j = 0$, we do the same for $x_j \nabla H_f(x)_j = 0$, we obtain the following iteration step:

$$x_j^{k+1} = \frac{x_j^k(\beta_j/\alpha_j)\sum_i L_{ij}\left[c_i \exp\left(-Lx_i^k\right) Lx_i^k\right] + p_j}{(\beta_j/\alpha_j)\sum_i L_{ij}\left[y_i - c_i \exp\left(-Lx_i^k\right)\left(1 - Lx_i^k\right)\right] + 1}. \tag{4.28}$$

This should perform better, since, for large values of (α_j/β_j), we get (approximately) p_j on the right hand side for the above equation. Following arguments presented by Case *et al.* [4], by choosing

$$w_j = \frac{1}{(\beta_j/\alpha_j)\sum_i L_{ij}\left[y_i - c_i \exp\left(-Lx_i^k\right)\left(1 - Lx_i^k\right)\right] + 1} \tag{4.29}$$

to be the weight of the prior relative to the object, the gamma-prior version of the convex algorithm becomes

$$x_j^{k+1} = (1 - w_j)\frac{x_j^k \sum_i L_{ij} c_i \exp\left(-Lx_i^k\right) Lx_i^k}{\sum_i L_{ij}\left[y_i - c_i \exp\left(-Lx_i^k\right)\left(1 - Lx_i^k\right)\right]} + w_j p_j. \tag{4.30}$$

In order to provide a suitable comparison with the BITAB algorithm, the Convex updates [see (4.23) and (4.30)] were modified by applying the same upper and lower pixel value constraints, i.e., the b_js and a_js, at every iteration. The details of this modification are described in Section V-A.

V. Methods

A. Simulation

We used the three-dimensional mathematical cardiac and torso (MCAT) phantom [26], [27] to simulate Tc^{99m} attenuation maps for a large female patient with a maximal across the body dimension of 38 cm. The linear attenuation coefficients for cortical bone, spine, lungs, breast and soft tissue were 0.212, 0.169, 0.045, 0.153, and 0.153 cm^{-1}, respectively. The attenuation maps were sampled at 128 × 128 pixels with a pixel size of 0.317 cm/pixel. The attenuation maps were blurred with an anti-aliasing Gaussian kernel (standard deviation of 1.4 pixels or 0.444 cm) to approximate the resolution of the attenuation maps acquired with our system [6]. Our standard imaging geometry for transmission imaging uses a 65 cm fan beam collimator, a circular camera orbit, and a radius of rotation (ROR) of 25 cm. Line integrals of the attenuation map were obtained over 360° (60 angles) on a 128 × 128 grid for this fan beam geometry and then folded down to 64 bins per view to simulate the effects of sampling. Noise-free transmission projections y_i were then obtained by applying an artificial blank scan to these line-integrals, i.e., $c_i \exp(-(Lx)_i)$. Poisson noise was added to this data set by using $c_i \exp(-(Lx)_i)$ as expected values of the Poisson distribution from which pseudo-random noise realizations were generated. Three blank scan rates were simulated; a normal blank scan of 500 counts per bin along with two other low counts scans of 250 and 125 counts per bin. Noise in the blank scans was not simulated since they are typically acquired over longer periods of time than a conventional patient transmission scan. Twenty five independent noise realizations were obtained in order to compute fidelity measures detailed in Section V-A1. Note that emission crosstalk was not included in these simulations.

The 25 noise-realizations were reconstructed using ML-G, Convex, and BITAB algorithms with and without noise regularization. Body outline was used as support [2], [4] in all cases wherein only those pixels j within the confines of the body outline were reconstructed; pixels outside the body were set to zero. In these simulations, we used the exact body-outline computed from the true attenuation maps by simple thresholding [28]. Reconstructions using 30 iterations of the unregularized form of ML-G [(3.18) and (3.19)], 30 iterations of the Convex algorithm (4.23) and two iterations of BITAB [(2.6), (2.7), and (2.17)] without any regularization (regularization parameter $\hat{\beta}$ was set to zero) were first obtained, with $r = 10$. Note that since down-scatter was not simulated, the background term s_i in (2.17) is set to zero. The BITAB reconstructions used 15 subsets of four views each covering 360° with sequential subsets separated as much as possible. Note that the number of BITAB iterations were chosen to approximately match those of the ML-G and convex iterates (two full BITAB iterations with 15 subsets matched the 30 iterations chosen for ML-G and convex algorithms). Additionally, we chose flat upper and lower bounds, i.e., $b_j = 0.25\ \text{cm}^{-1}$ and $a_j = 0\ \text{cm}^{-1}$ at all pixels j in implementing the BITAB reconstructions. A generous upper limit of 0.25 cm^{-1} was selected for convenience, accounting for the largest linear attenuation coefficient of 0.212 cm^{-1} used, which in these simulations represented cortical bone.

To enable a fair comparison with the proposed BITAB algorithm, the Convex algorithm was modified to include upper and lower pixel value constraints. This was accomplished by first performing the standard update (4.23) and then setting any pixel value below the lower bound to a_j while any pixel value above the upper bound was set to b_j at each iteration. For these Convex reconstructions, the same a_js and b_js, i.e., $b_j = 0.25\ \text{cm}^{-1}$ and $a_j = 0\ \text{cm}^{-1}$ were used to constrain the reconstructions at each iteration.

Next, the data sets were reconstructed using 30 iterations of the modified gamma-prior version of ML-G (3.20) which is our

$$x_j^{k+1} = x_j^k - x_j^k \frac{\left[\sum_i L_{ij} x_j^k \left(y_i - c_i \exp\left(-Lx_i^k\right)\right)\right] + \left(x_j^k - p_j\right)\alpha_j/\beta_j}{\left[\sum_i L_{ij} x_j^k Lx_i^k c_i \exp\left(-Lx_i^k\right)\right] + (\alpha_j/\beta_j)p_j} \tag{4.27}$$

current clinical standard. As mentioned in Section III, the prior p was formed by assigning soft-tissue linear attenuation coefficients to all pixels enclosed within the body-outline. The spatially varying weighting function w_j that is used to combine both the ML-G estimate and the prior was chosen to have the following form [4]:

$$w_j = \frac{w_0}{1 + \exp[(r_{\text{fsr}} - r_j)/\delta]} \tag{5.31}$$

where

r_j radius of pixel j from the center of rotation;
r_{fsr} radius of the FSR;
δ distance over which w_j changes by a factor of $1 + e$
w_0 maximum weight given to the prior.

For small weights of the prior ($w_0 < 0.2$ determined experimentally) [4], use of the gamma prior (3.20) maintains the attenuation line-integrals. For this application we chose $w_0 = 0.1$.

The gamma-prior version of the Convex algorithm was (4.30) next used to reconstruct the simulated data sets (30 iterations). Details about the prior p_j and weighting function w_j are as explained above. As was done in the un-regularized case, the regularized Convex iterates were again constrained by the upper and lower bounds ($b_j = 0.25$ cm^{-1} and $a_j = 0$ cm^{-1}) at each iteration.

Finally, reconstructions using two iterations of the regularized BITAB using 15 subsets of four views each were also obtained using the afore mentioned prior p. The regularization parameter $\hat{\beta}$ in (2.6), (2.7) and (2.17) was also chosen to vary spatially in a similar manner to w_j, i.e.,

$$\hat{\beta}_j = \frac{\hat{\beta}_0}{1 + \exp[(r_{\text{fsr}} - r_j)/\delta]} \tag{5.32}$$

where $\hat{\beta}_0 = 0.0067$ is the maximum weight given to the prior. Note that the regularization parameter was divided by the number of subsets to match that used in the gamma-prior versions of the ML-G and convex algorithms. Again, with this spatially varying form, very little weight is given to the prior within the FSR. The deleterious effects of truncation outside the FSR are compensated for by giving greater weight to an anatomically correct prior. Flat upper and lower bounds of $b_j = 0.25$ cm^{-1} and $a_j = 0$ cm^{-1} were chosen for all pixels j enclosed within the body-outline to restrict the over-estimation of attenuation coefficients due to inconsistent data.

1) Fidelity Criteria: Since compensation for the effects of nonuniform attenuation in emission reconstructions requires computation of line-integrals rather than pixel values themselves, measures such as absolute bias and variance were computed for line-integrals through the attenuation map centered on a location in the left-ventricle. These measures of fidelity were computed from 25 noise realizations for each reconstruction strategy as follows. Let $\mathcal{LI}(n)$ be any line-integral from the nth noise realization, $n = 1, \ldots, N = 25$. We then define the average line-integral as

$$\widehat{\mathcal{LI}} = \frac{1}{N} \sum_{n=1}^{N} \mathcal{LI}(n). \tag{5.33}$$

If $\mathcal{LI}(\text{truth})$ represents the true value for $\widehat{\mathcal{LI}}$, the absolute bias in the different reconstructions strategies is computed as

$$\text{Absolute bias} = |\widehat{\mathcal{LI}} - \mathcal{LI}(\text{truth})| \tag{5.34}$$

while the sample variance of line-integrals is

$$\sigma^2 = \frac{N}{N-1} \left[\frac{1}{N} \sum_{n=1}^{N} \{\mathcal{LI}(n)\}^2 - \{\widehat{\mathcal{LI}}\}^2 \right]. \tag{5.35}$$

Line-integrals passing through the center of a representative slice were used in computing bias and variance measures. Absolute bias and variance were computed separately for all line-integrals and averaged for each reconstruction strategy.

B. Phantom Study

The Anthropomorphic Torso phantom (Data Spectrum Corporation, Hillsborough, NC), with a cardiac insert and breast attenuator to simulate a female torso, was imaged using the three-headed PRISM-3000 SPECT imaging system with a Gd^{153} line source, to provide actual data with knowledge of the true values of the attenuation coefficients. A simultaneous emission/transmission protocol [1], [4], [7] was employed where, two parallel hole collimators acquired emission images while the third head, with a 65 cm fan-beam collimator opposed to a Gd^{153} line source, acquired transmission projections. Two separate studies were acquired where the activity levels in the phantom were varied to simulate different levels of difficulty with respect to the contamination of the transmission acquisitions in the presence of surrounding activity [29]. The concentrations used in the phantom for the two studies were as follows.

1) Activity in the heart walls was 4.2 mCi of Tc^{99m}/liter, with no background activity in the surrounding regions; and
2) Activity in the heart walls and liver was 4.2 mCi of Tc^{99m}/liter; while the activity in the rest of the phantom, excluding the lungs, was at 1/12th the activity of the heart and liver.

The activity levels and acquisition times were selected to approximate clinical acquisitions. The window settings for the emission data were: Tc^{99m} photopeak window centered at 140 keV with a width of 15%, a large Tc^{99m} Compton scatter window centered at 106 keV ± 25% width for determining the body outline and another window at 123 keV ± 4% width for performing Ogawa [30] scatter correction of the photo-peak data. The window settings for the transmission data consisted of a Gd^{153} photo peak window at 100 keV ± 15% width and two scatter windows centered at 123 keV ± 4% width and 84 keV ± 6% width for performing Ogawa scatter correction of the transmission photo-peak data. A circular orbit of 26 cm was employed and a total of 120 projection frames of 64 × 64 pixels with a pixel size of 0.634 cm were acquired over 360° with an acquisition time of 8 s/frame. Prior to these acquisitions, a single flood image was acquired, serving as the blank scan. The transmission and flood projections were corrected for resolving time and physical decay. The Tc^{99m} crosstalk in the Gd^{153} transmission projection data was estimated using Ogawa's

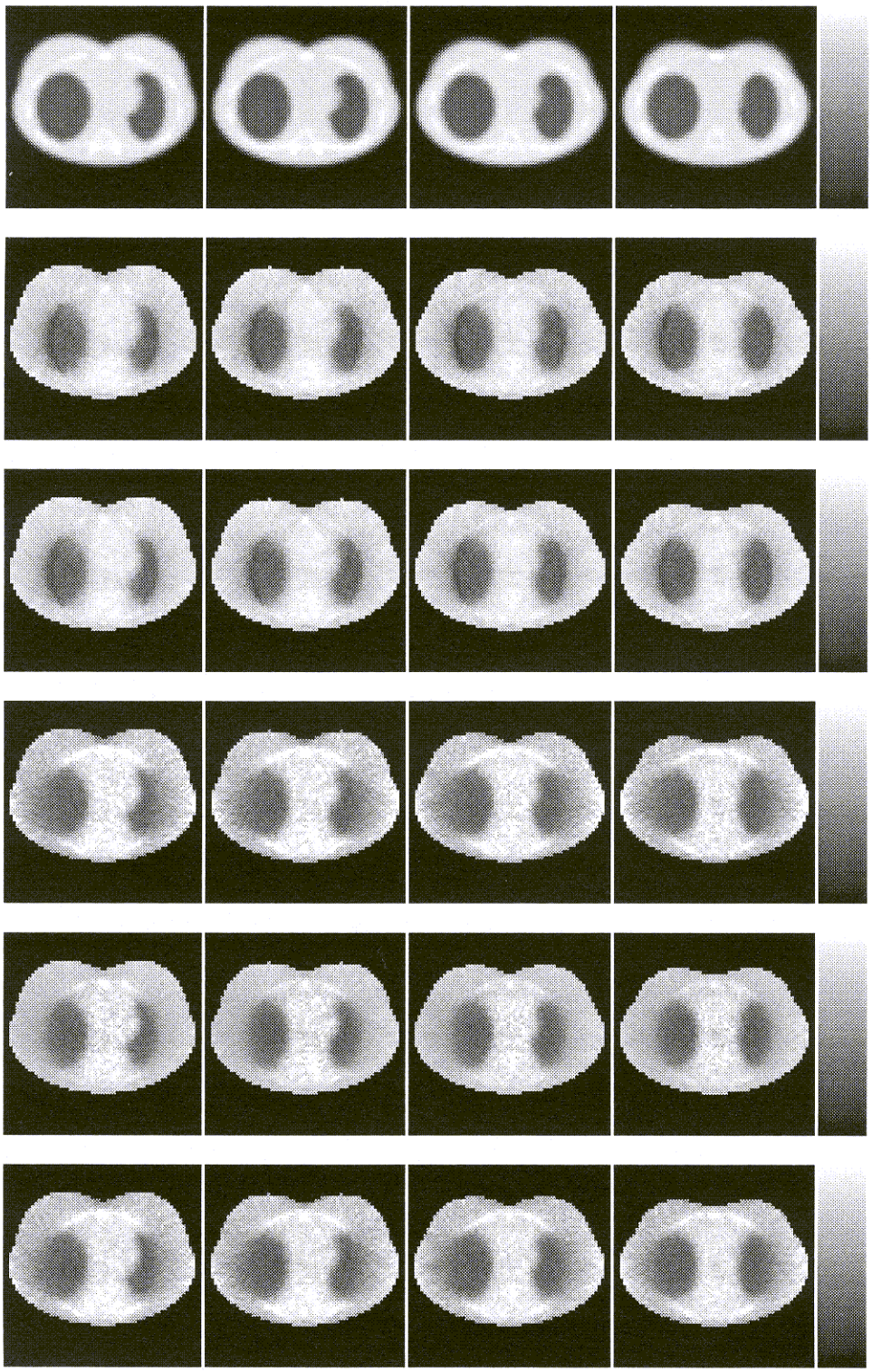

Fig. 1. Transverse slices of the reconstructed MCAT attenuation maps for the low count case. The slices shown are taken from the mean images formed from 25 noise realizations. The true slices are shown in row one while rows two through seven represent images for the following reconstruction algorithms: unregularized BITAB, BITAB, ML-G, ML-G with gamma prior, Convex, and Convex with gamma prior.

triple energy window method. The estimated emission crosstalk was subtracted prior to applying the gamma-prior-based ML-G and Convex algorithms, while the BITAB algorithm includes this estimate as s_i in (2.17).

The transmission projections were reconstructed using 30 iterations of the gamma-prior versions of ML-G and the Convex algorithms as well as two iterations of BITAB with 15 subsets of eight views each, with $r = 10$. To reduce the effects of truncation, all algorithms used an estimate of the body-outline as support, reconstructing only those pixels confined within the outline. A convex body outline was estimated from Compton scattered projection data by simple thresholding [4], [31], [32].

Before estimating this outline, the projection data was folded down to half the number of acquisition angles to reduce the impact of noise. Since the true body outline is a smooth contour, it was finally Fourier filtered to exclude the higher frequency components [33]. The filter chosen to suppress the high-frequency terms had the following form:

$$F(f) = \frac{1}{1 + \exp(f - f_o)} \tag{5.36}$$

where $f_o = 8$ is the cutoff frequency. This filtering greatly reduces the influence of noise providing smoother outlines. The pixel-by-pixel prior estimate was formed by assigning soft-tissue linear attenuation coefficients to all pixels enclosed within the body outline. A known map for the table was also included within this attenuation map to complete the prior estimate. The BITAB reconstructions of the map of Gd^{153} attenuation coefficients were obtained with $\hat{\beta}_o$ =0.1/(15 subsets) = 0.0067 scaled to match the regularization ($w_o = 0.1$) applied to the gamma-prior versions of ML-G and convex algorithms. Also, bounds of $a_j = 0$ cm^{-1} and $b_j = 0.35$ cm^{-1} were set at all pixels within the FSR. The remaining pixels outside the FSR had $a_j = 0$ cm^{-1} and $b_j = 0.2$ cm^{-1}. The assumption here is that with proper positioning, highly attenuating structures such as the teflon spinal insert with an expected attenuation coefficient of 0.30 cm^{-1} [34] are enclosed within the FSR, with water being present outside the FSR. Besides, by restricting b_j to 0.2 cm^{-1} outside the FSR, it is possible to restrict the over-estimation of attenuation coefficients that typically result when reconstructing truncated data. The Convex iterates were again constrained to lie within the a_js and b_js at the end of each iteration. Please also note that since phantom study-I had no background activity present, it was difficult to obtain an acceptable estimate of the body outline. As a result, we used the body outline estimated from the acquisition that had extra-cardiac activity present, i.e., phantom study-II. Care was taken to ensure that both studies were registered with one another, thus minimizing any mismatch between the prior estimate and the standard updates for all 3 reconstruction strategies for phantom study-I.

C. Patient Study

A patient study has also been included to demonstrate the applicability of using the BITAB algorithm to reconstruct patient specific attenuation maps. A circular orbit of 27 cm was employed and a total of 60 projection frames of 64 × 64 pixels with a pixel size of 0.634 cm were acquired over 360° with an acquisition time of 16 sec/frame. The number of projection frames were halved and the acquisition time per frame doubled, in order to get better count statistics. All other data acquisition and reconstruction details are as described in Section V-B except that BITAB reconstructions used groupings of 4 angles per subset to have the same number subsets (15) as the phantom and simulation studies.

VI. Results and Discussion

A. Simulation Results

Fig. 1 shows reconstructed transverse slices of the MCAT attenuation map for the six different reconstruction strategies considered compared against the true MCAT transmission map. The images shown are mean images of reconstructions averaged over 25 noise realizations for the low count simulation where the blank scan counts per bin was assumed to be 125 counts. Visually, ML-G reconstructions without any regularization appear the noisiest. As one would expect, inclusion of the gamma prior in the ML-G algorithm provides smoother attenuation maps. The BITAB and Convex reconstructions both with and without regularization also provide reasonably smooth attenuation maps.

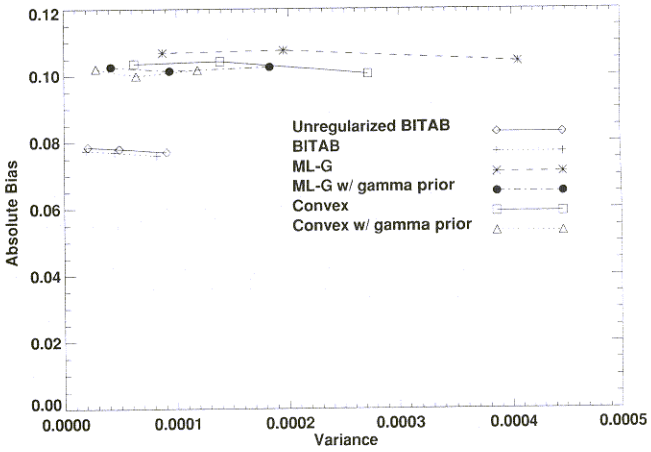

Fig. 2. Plot of absolute bias versus variance for the line-integrals estimated for each of the six reconstruction strategies considered for the three different count levels (Note: lowest count levels are to the right).

To quantify any differences that might exist between the six reconstruction strategies, a plot of the absolute bias versus variance of the estimated line-integrals is shown in Fig. 2 for the three different count levels considered. In all six curves, the data point with the highest variance corresponds to the low count study, where the blank scan equals 125 counts/bin. Similarly, the normal study with 500 counts/bin correlates with the data point having the least variance. In the absence of any regularization, both BITAB and Convex algorithms have lower variances in comparison to the ML-G algorithm. However, the BITAB reconstructions have lower absolute bias levels than the remaining two algorithms. When regularization is included in the reconstructions, as expected, an additional reduction in the variance levels is seen, in comparison to the un-regularized case. However, the key observation in this simulation appears to be lower bias levels provided by the BITAB reconstructions. This may in part be explained by the fact that the proposed algorithm makes the iterates stay away from the bounds as much as possible. On the other hand, the Convex iterates with enforced upper and lower bounds at every iteration would lead to many of the pixel values equal to the boundary values. In other words, if the ML solution does not have any of the applied boundary values, enforcing a clipping method as was done with the Convex algorithm may impose them. As a result, it might take many more iterations to move away from these boundary values and proceed toward the ML solution.

B. Torso Phantom Results

Attenuation maps reconstructed from Gd^{153} transmission data with BITAB, Convex, and ML-G algorithms, were scaled

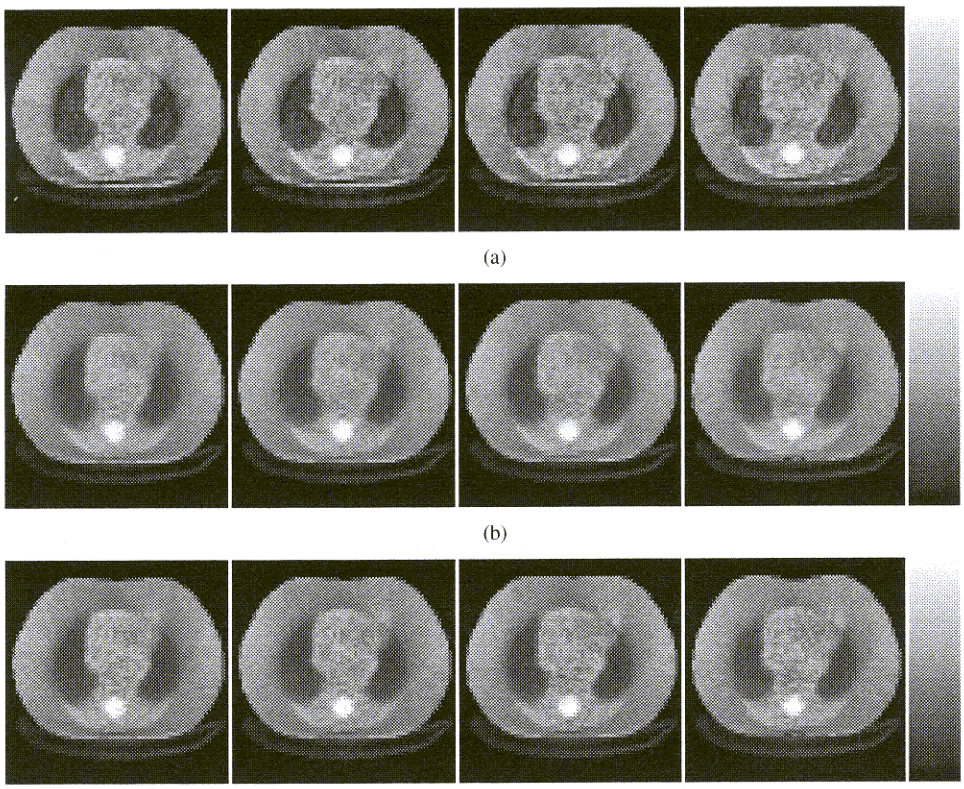

(a) (b) (c)

Fig. 3. Transverse slices of the reconstructed attenuation maps for phantom study I. (a) BITAB, (b) gamma-prior-based Convex, and (c) ML-G reconstructions.

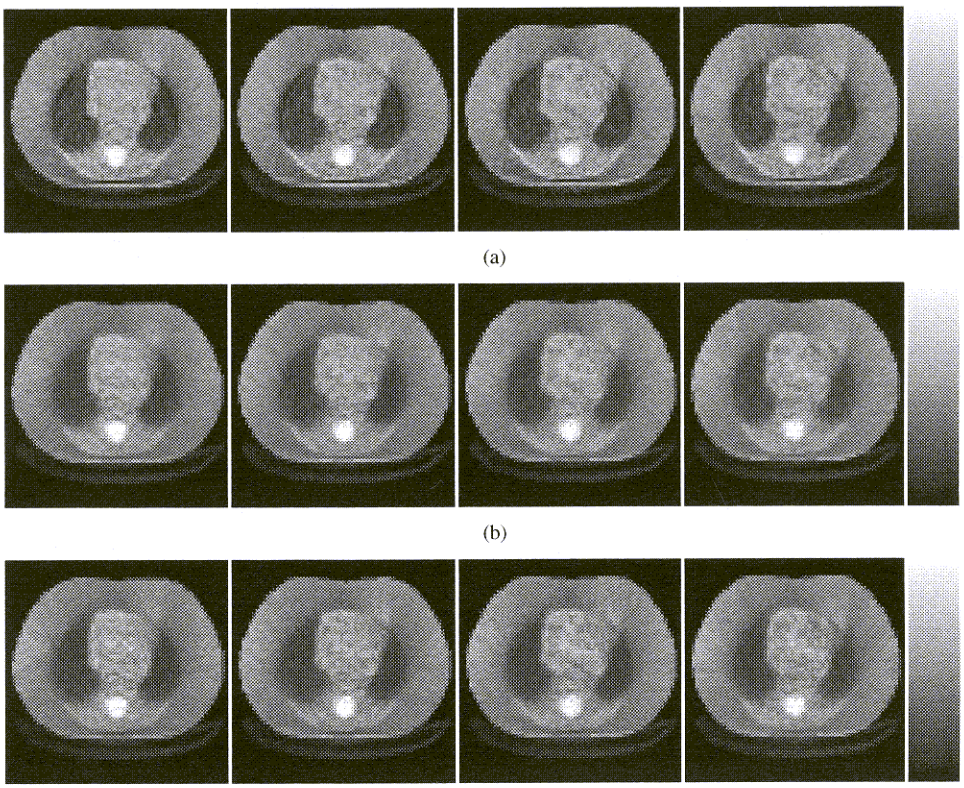

(a) (b) (c)

Fig. 4. Transverse slices of the reconstructed attenuation maps for phantom study II. (a) BITAB, (b) gamma-prior-based Convex, and (c) ML-G reconstructions.

for Tc^{99m} using a multiplication factor of 0.9 [35]. Transverse slices of the reconstructed attenuation maps for phantom studies I and II are illustrated in Figs. 3 and 4, respectively. Table I compares the measured linear attenuation coefficients

TABLE I
THE AVERAGE OBSERVED LINEAR ATTENUATION COEFFICIENTS FOR THE TORSO PHANTOM STUDIES ARE TABULATED FOR BITAB, ML-G, AND CONVEX RECONSTRUCTIONS AND COMPARED AGAINST THE EXPECTED VALUES. HERE FSR STANDS FOR FULLY SAMPLED REGION

	Tissue	*BITAB*	*ML-G*	*Convex*	*Truth*
Phantom Study I	Water (inside FSR)	0.153	0.154	0.155	0.153 ± 0.002
	Water (outside FSR)	0.155	0.163	0.160	0.153 ± 0.002
	Lungs	0.051	0.054	0.058	0.049 ± 0.003
	Spine	0.290	0.301	0.298	0.291 ± 0.005
Phantom Study II	Water (inside FSR)	0.154	0.155	0.155	0.153 ± 0.002
	Water (outside FSR)	0.154	0.158	0.153	0.153 ± 0.002
	Lungs	0.047	0.058	0.060	0.049 ± 0.003
	Spine	0.302	0.312	0.311	0.291 ± 0.005

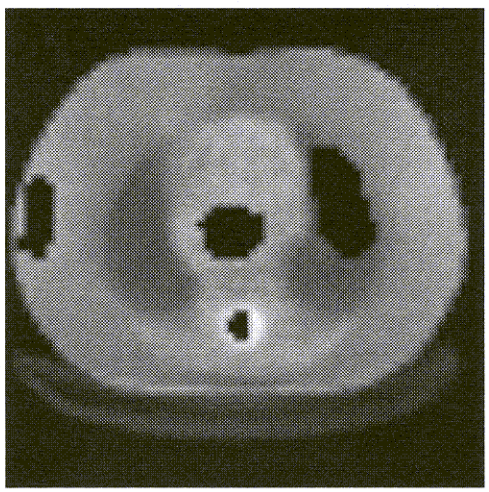

Fig. 5. Illustration of ROIs used to compute reconstructed linear attenuation coefficients. The ROIs shown in black have been superimposed onto the reconstructed transmission slice.

for all algorithms. The tabulated attenuation coefficients were obtained by drawing regions of interest (ROIs) on the reconstructed transmission maps and averaging the coefficients within the ROIs. The ROIs used for estimating the linear attenuation coefficients are displayed in Fig. 5, superimposed on the reconstructed transmission slice. Measurements were made in lung, water and spinal areas within the FSR. In addition, the attenuation coefficient for water was also measured at ROIs located outside the FSR. To facilitate comparison between the algorithms, experimentally observed narrow beam attenuation coefficients published by Jaszczak *et al.*, [34] have been reproduced in Table I. In both these phantom studies, ML-G, Convex, and BITAB reconstructions show fairly good agreement with the experimentally observed values, indicating that all three algorithms perform similarly.

C. Patient Study Results

Since the "true" attenuation map is unknown, only a qualitative analysis is presented. Fig. 6 compares the profiles as well as reconstructed transverse slices for the patient study acquired at our clinic. Transverse slices for ML-G, Convex, and BITAB reconstructions appear very similar visually. However, inspection of the profiles through the slices reveal that in areas outside the FSR, BITAB algorithm through its bounds, tends to limit the over-estimation of attenuation coefficients, in contrast to the ML-G and Convex reconstructions.

VII. CONCLUSION

A new rescaled block iterative algorithm that incorporates upper and lower bounds called the BITAB has been presented and its application toward reconstructing truncated fan beam projections studied through computer simulations, phantom, and clinical patient studies. MCAT phantom simulations reveal that the BITAB algorithm in conjunction with reasonably selected prior upper and lower bounds has the potential to improve the accuracy of the reconstructed attenuation coefficients from truncated fan beam transmission projections. Since the range of attenuation coefficients is typically known, the BITAB algorithm through use of prior bounds on the reconstructions can help alleviate some of the inaccuracies inherent in fan beam transmission imaging. By using appropriate bounds, it is possible to reduce the bias in the coefficients that typically results from reconstructing truncated fan beam projections. The BITAB algorithm was also studied within a clinical setting, where confounding factors such as Tc^{99m} crosstalk, resolving time limitations, physical decay, and noise introduced by the lower count statistics, further degrade the accuracy of the attenuation maps reconstructed from truncated fan beam projections. With reasonably selected upper and lower bounds, the BITAB algorithm can prevent the over-estimation of attenuation coefficients outside the FSR.

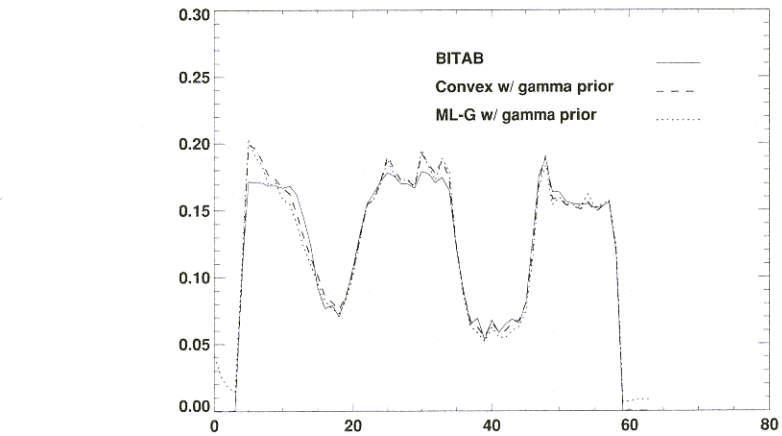

(a)

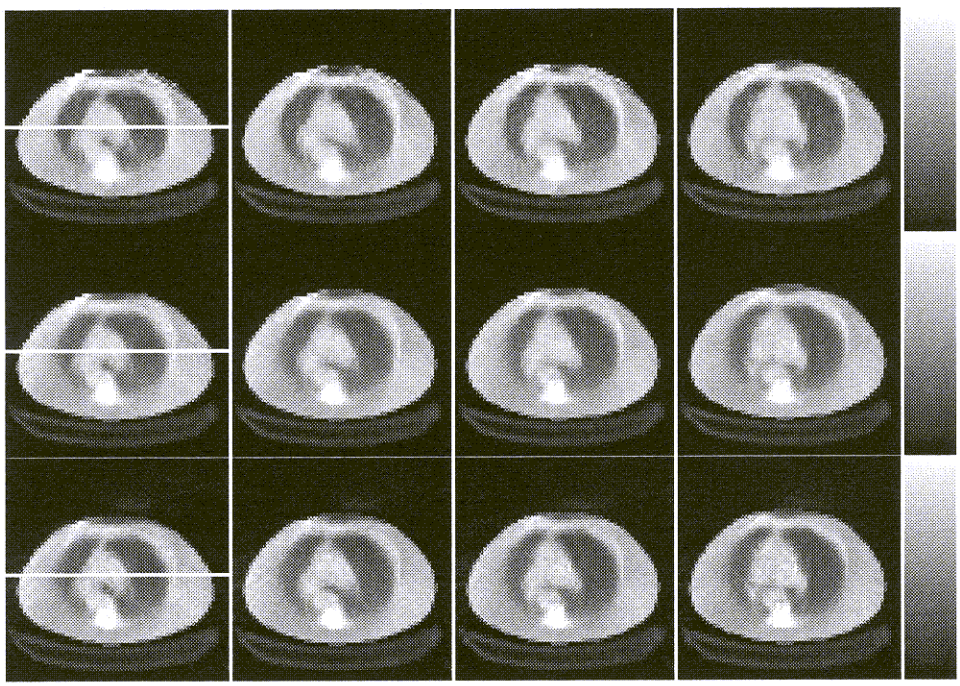

(b)

Fig. 6. Comparison of BITAB and gamma-prior-based Convex and ML-G reconstructions for the patient study. (a) Shows profiles through the lungs while (b) shows transverse slices of the attenuation maps. Rows one, two, and three represent slices for BITAB and gamma-prior-based Convex and ML-G algorithms, respectively. Note that the profiles shown in (a) correspond to the horizontal line drawn across the first transverse slice of each reconstruction strategy.

APPENDIX
BREGMAN FUNCTIONS

Let S be an open convex set in R^J, with closure $\bar{S}$. Let $f : \bar{S} \to R$ and define $D_f(x,z) : \bar{S} \times S \to R$ by

$$D_f(x,z) = f(x) - f(z) - \langle \nabla f(z), x - z \rangle.$$

Following [36], we say that f is a Bregman function with zone S if the following conditions are satisfied.

B1: f is continuous and differentiable on S;
B2: f is twice continuously differentiable on S and its Hessian matrix $\nabla^2 f(x)$ is positive-definite for all x in S;
B3: for each fixed x in $\bar{S}$ the level sets $\{z \mid D_f(x,z) \leq \alpha\}$ are bounded and for each fixed z in S the level sets $\{x \mid D_f(x,z) \leq \alpha\}$ are bounded;
B4: if $y^k \in S$ and $\{y^k\} \to y^*$ then $D_f(y^*, y^k) \to 0$;
B5: if $x^k \in \bar{S}$ and $y^k \in S$, with $\{x^k\}$ bounded, $\{y^k\} \to y^*$ and $D_f(x^k, y^k) \to 0$, then $\{x^k\} \to y^*$.

Then, D_f is the Bregman distance associated with the Bregman function f. Note that condition B2 is often replaced with the weaker condition that f be continuously differentiable on S.

REFERENCES

[1] E. P. Ficaro, J. A. Fessler, R. J. Ackermann, W. L. Rogers, J. R. Corbett, and M. Schwaiger, "Simultaneous transmission-emission Thallium-201 cardiac SPECT: Effect of attenuation correction on myocardial tracer distribution," *J. Nucl. Med.*, vol. 36, pp. 921–931, June 1995.
[2] T.-S. Pan, M. A. King, B. C. Penney, N. Rajeevan, D.-S. Luo, and J. A. Case, "Reduction of truncation artifacts in fan beam transmission by using parallel beam emission data," *IEEE Trans. Nucl. Sci.*, vol. 42, pp. 1310–1319, Aug. 1995.
[3] M. A. King, B. M. W. Tsui, and T.-S. Pan, "Attenuation compensation for cardiac single-photon emission computed tomographic imaging: Part 1. Imaging of attenuation and methods of estimating attenuation maps," *J. Nucl. Cardiol.*, vol. 2, pp. 513–524, Nov. 1995.

[4] J. A. Case, T.-S. Pan, M. A. King, D.-S. Luo, B. C. Penney, and S. Z. Rabin, "Reduction of truncation artifacts in fan beam transmission using a spatially varying gamma prior," *IEEE Trans. Nucl. Sci.*, vol. 42, pp. 2260–2265, Dec. 1995.

[5] R. J. Jaszczak, D. R. Gilland, J. W. McCormick, C. Scarfone, and R. E. Coleman, "The effect of truncation reduction in fan beam transmission for attenuation correction of cardiac SPECT," *IEEE Trans. Nucl. Sci.*, vol. 43, pp. 2255–2262, Aug. 1996.

[6] D.-S. Luo, M. A. King, T.-S. Pan, and W. Xia, "Evaluation of the effects of patient arm attenuation in SPECT cardiac perfusion imaging," *IEEE Trans. Nucl. Sci.*, vol. 43, pp. 3291–3299, Dec. 1996.

[7] L. R. Barnden, P. L. Ong, and C. C. Rowe, "Simultaneous emission transmission tomography using technetium-99m for both emission and transmission," *Eur. J. Nucl. Med.*, vol. 24, pp. 1390–1397, Nov. 1997.

[8] G. T. Gullberg, H. T. Morgan, G. L. Zeng, P. E. Christian, E. V. R. Di Bella, C.-H. Tung, P. J. Maniawski, Y.-L. Hsieh, and F. L. Datz, "The design and performance of a simultaneous transmission and emission tomography system," *IEEE Trans. Nucl. Sci.*, vol. 45, pp. 1676–1698, June 1998.

[9] Z. Liang and J. Ye, "Reconstruction of object-specific attenuation map for quantitative SPECT," in *Conf Rec. IEEE Medical Imaging Conf.*, San Francisco, CA, Nov. 1993, pp. 1231–1235.

[10] G. T. Gullberg, C.-H. Tung, B. M. W. Tsui, and J. R. Perry, "Correction for truncated fan beam projections in cardiac SPECT imaging," *Eur. J. Nucl. Med.*, vol. 15, p. 559 (abstract), May 1989.

[11] B. M. W. Tsui, D. D. Zhao, P. Vemon, D. Nowak, J. R. Perry, and W. H. McCartney, "Cardiac SPECT reconstructions with truncated projections in different SPECT system designs," *J. Nucl. Med.*, vol. 33, p. 831 (abstract), May 1992.

[12] N. Rajeevan, B. C. Penney, and M. A. King, "Improving the quantitative accuracy and resolution of thoracic SPECT imaging," in *Conf Rec. IEEE Medical Imaging Conf.*, San Francisco, CA, Nov. 1993, pp. 1345–1348.

[13] W. Chang, S. Loncaric, G. Huang, and P. Sanpitak, "Asymmetrical fan beam transmission CT on SPECT system," *Phy. Med. Biol.*, pp. 913–928, May 1995.

[14] D. R. Gilland, H. Wang, R. E. Coleman, and R. J. Jaszczak, "Long focal length asymmetric fan beam collimation for transmission acquisition with a triple camera SPECT system," *IEEE Trans. Nucl. Sci.*, vol. 44, pp. 1191–1196, June 1997.

[15] D. R. Gilland, R. J. Jaszczak, T. G. Turkington, and R. E. Coleman, "Comparison of transmission acquisition approaches for SPECT nonuniform attenuation compensation," *IEEE Trans. Nucl. Sci.*, vol. 45, pp. 1244–1249, June 1998.

[16] M. A. King, D.-S. Luo, S. T. Dahlberg, and B. J. Villegas, "Transmission imaging of large attenuators using a slant hole collimator on a three-headed SPECT system," *Med. Phys.*, vol. 23, pp. 263–272, Feb. 1996.

[17] C. L. Byrne, "Block-iterative interior point optimization methods for image reconstruction from limited data," *Inverse Problems*, vol. 16, pp. 1405–1419, 2000.

[18] ——, "Block-iterative methods for image reconstruction from projections," *IEEE Trans. Image Processing*, vol. 5, pp. 792–794, May 1996.

[19] ——, "Accelerating the EMML algorithm and related iterative algorithms by rescaled block-iterative methods," *IEEE Trans. Image Processing*, vol. 7, pp. 100–109, Jan. 1998.

[20] ——, "Iterative algorithms for deconvolution and deblurring with constraints," *Inverse Problems*, vol. 14, pp. 1455–1467, 1999.

[21] ——, "Iterative image reconstruction algorithms based on cross-entropy minimization," *IEEE Trans. Image Processing*, vol. 2, pp. 96–103, Jan. 1993.

[22] K. Lange, M. Bahn, and R. Little, "A theoretical study of some maximum likelihood algorithms for emission and transmission tomography," *IEEE Trans. Med. Imag.*, vol. MI-6, pp. 106–114, June 1987.

[23] K. Lange and J. A. Fessler, "Globally convergent algorithms for maximum *a posteriori* transmission tomography," *IEEE Trans. Imag. Processing*, vol. 4, pp. 1430–1438, Oct. 1995.

[24] A. R. De Piero, "A modified expectation maximization algorithm for penalized likelihood estimation in emission tomography," *IEEE Trans. Med. Imag.*, vol. MI-14, pp. 132–137, Mar. 1987.

[25] H. Erdoğan and J. A. Fessler, "Ordered subsets algorithms for transmission tomography," *Phys. Med. Biol.*, vol. 44, pp. 2835–2851, 1999.

[26] B. M. W. Tsui, X. D. Zhao, G. K. Gregario, D. S. Lalush, E. C. Frey, R. E. Johnson, and W. H. McCartney, "Quantitative cardiac SPECT reconstruction with reduced image degradation due to patient anatomy," *IEEE Trans. Nucl. Sci.*, vol. 41, pp. 2838–2844, Dec. 1994.

[27] G. K. Gregario, B. M. W. Tsui, and G. T. Gullberg, "Effect of truncated projections on defect detection in attenuation compensated fan-beam cardiac SPECT," *J. Nucl. Med.*, vol. 39, pp. 166–175, Jan. 1998.

[28] N. Otsu, "A threshold selection method from gray-level histograms," *IEEE Trans. Syst., Man, Cybern.*, vol. SMC-9, pp. 62–66, Jan. 1979.

[29] E. N. Heller, P. DeMan, Y.-H. Liu, D. P. Dione, I. G. Zubal, F. J. T. Wackers, and A. J. Sinusas, "Extracardiac activity complicates quantitative cardiac SPECT imaging using a simultaneous transmission-emission approach," *J. Nucl. Med.*, vol. 38, pp. 1882–1890, Dec. 1997.

[30] K. Ogawa, Y. Harata, T. Ichihara, A. Kubo, and S. Hashimoto, "A practical method for position-dependent compton-scatter correction in single photon emission CT," *IEEE Trans. Med. Imag.*, vol. 10, pp. 408–412, Sept. 1991.

[31] T.-S. Pan, M. A. King, D. J. de Vries, and M. Ljunberg, "Segmentation of the body and lungs from compton scatter and photopeak window data in SPECT: A Monte-Carlo investigation," *IEEE Trans. Med. Imag.*, vol. 15, no. 1, pp. 13–24, Feb. 1996.

[32] T.-S. Pan, M. A. King, D.-S. Luo, S. T. Dahlberg, and B. J. Villegas, "Estimation of attenuation maps from single photon-emission computed tomographic images of technetium 99m-labeled sestamibi," *J. Nucl. Cardiol.*, vol. 4, no. 1, pp. 42–51, Jan./Feb. 1997.

[33] J. A. Case, M. A. King, D.-S. Luo, E. J. Soares, and M. S. Z. Rabin, "Determination of concave body outlines directly from SPECT projection data," in *Conf. Rec. IEEE Medical Imaging Conf.*, Oct. 1995, pp. 944–948.

[34] R. J. Jaszczak, D. R. Gilland, M. W. Hanson, S. Jang, K. L. Greer, and R. E. Coleman, "Fast transmission CT for determining attenuation maps using a collimated line source, rotatable air-copper-lead attenuators and fan beam collimation," *J. Nucl. Med.*, vol. 34, pp. 1577–1585, Sept. 1993.

[35] A. Welch, G. T. Gullberg, P. E. Christian, and F. L. Datz, "A comparison of Gd/Tc versus Tc/Tl simultaneous transmission and emission imaging using both single and triple detector fan beam SPECT systems," *IEEE Trans. Nucl. Sci.*, vol. 41, pp. 2779–2786, Dec. 1994.

[36] Y. Censor, A. Iusem, and S. Zenios, "An interior point method with Bregman functions for the variational inequality problem with paramonotone operators," *Mathematical Programming*, vol. 81, pp. 373–400, 1998.